Radiation damage in diopside and calcite crystals from uranothorianite inclusions

Anne-Magali Seydoux-Guillaume [a,*], Jean-Marc Montel [a], Richard Wirth [b], Bernard Moine [a]

[a] LMTG, CNRS, Université de Toulouse, IRD, OMP, 14 avenue Edouard Belin, 31400 Toulouse, France
[b] GeoForschungsZentrum (GFZ) Potsdam-Division 4, Telegrafenberg, D-14473 Potsdam, Germany

ARTICLE INFO

ABSTRACT

Combining observation and simulation, radiohalos formed around uranothorianite (UTh) from the Tranomaro granulitic skarns (SE-Madagascar) were studied. These structures consist of UTh grains surrounded by both aluminous diopside (Cpx) and calcite (Cc_1) crystals. Optical microscope and Scanning Electron Microscope (SEM) images revealed (1) the presence of radiating cracks around the UTh probably due to swelling of the metamict UTh, (2) a diffuse optical halo at the Cc_1/UTh interface, and (3) a wide "reaction zone" at the Cpx/UTh interface, composed of "secondary calcite" (Cc_2) with low temperature sheet silicate from the smectite (φ) group. Samples prepared across various interfaces using Focused Ion Beam (FIB) were investigated by Transmission Electron Microscope (TEM). In contrast to SEM observations, there is no direct contact between Cc_1 and UTh. From Cc_1 to UTh, we found: (1) a large (~200–300 nm) amorphous zone (A), enriched in U, Th and Ca, but without Si; (2) a chain (B) of very small (~20 nm) ThO_2 crystals; (3) another amorphous zone (C), which, in contrast to zone A is enriched in Si; and (4) another zone (D) made of small amorphous Si-rich "bubbles". The organization is similar for the UTh–Cc_2 interface. The presence of hydrous minerals (smectite) and carbonate (calcite) in reaction zone and in cracks, the presence of Pb-rich inclusions in secondary calcite, the abundance of fluid inclusions in the porous layer in calcite, the dissociation of U and Th in the calcite–uranothorianite layer, and the ThO_2 chains along interfaces, are strong indications that low-temperature crystallization was promoted by a fluid phase. SRIM simulation was used to calculate the effect of α and recoil particles of the three decay chains, in Cpx, Cc and UTh. The thickness of the damaged area calculated for α in Cpx and Cc are similar to the widths of the recrystallized areas observed in thin section (~30 µm). Corrected with the "wandering recoil effect", the size of the damaged area calculated for recoil nuclei in Cc (~50–60 nm) is ~multiplied by 3 and is in rather good agreement with the thickness of the totally amorphous layer at the Cc–UTh interface (~200 nm). Finally, it is emphasized that radiohalos are a point of chemical and physical weakness in a rock and probably a starting point for alteration.

1. Introduction

During geological time, U- and Th-rich minerals accumulate radiation damage, mainly from α decay. Such damage destroys to a variable extent the host crystal network, leading to an amorphous structure, called metamict state (summary in Ewing, 1994). Damage is caused by three types of particles. First, α particles, which are energetic (4–8 MeV), penetrative, (10–20 µm), but not very destructive (about 100 displacement/particle); second, recoil nuclei (daughter nuclei), which are less energetic (100–400 keV), less penetrative (20–50 nm), but more destructive (800–2000 displacement/particle); finally, fission nuclei, which are very energetic (150–200 MeV), very destructive (fission tracks are 10–20 µm long and 5–10 nm diameter, and made of several ten thousands displacements), but very rare (0.0005% of ^{238}U decays). Submitted to natural radiation damages, i.e. accumulated over a long time, minerals react differently: many

minerals, like zircon (review in Ewing et al., 2003) or allanite (Headley et al., 1981; Janeczek and Eby, 1993), become amorphous (metamict), whereas some remain crystalline such as monazite (Meldrum et al., 1998; Ewing and Wang, 2002; Seydoux-Guillaume et al., 2002; 2004; reviews in Ewing et al., 2003) or apatite (Linberg and Ingram, 1964; review in Ewing and Wang, 2002).

Radiation damage in radioactive minerals has been studied in the geosciences for two main reasons. First, U–Th-rich minerals are used for U–Th–Pb dating, and it is essential to understand the effects of radiation damages on lead retentivity (Lumpkin et al., 1986a; Davis and Krogh, 2000; Romer, 2003). Second, the effect of long-term accumulation of radiation damage is a key parameter for assessing the durability of ceramics that could be used as nuclear-waste forms (Ewing, 1975; Ewing et al., 1988; Ewing et al., 1995; Weber et al., 1998).

Four strategies are used to study radioactive damage in minerals (see review in Ewing et al., 2000): (1) external irradiation by ion beams (e.g. Wang and Ewing, 1992; Meldrum et al., 1998); (2) atomistic simulations (e.g. Crocombette and Ghaleb, 2001; Trachenko et al., 2001); (3) synthesis of doped-crystal with short-lived isotopes (e.g. Begg et al.,

* Corresponding author. Tel.: +33 5 61 33 25 97.
  E-mail address: seydoux@lmtg.obs-mip.fr (A.-M. Seydoux-Guillaume).
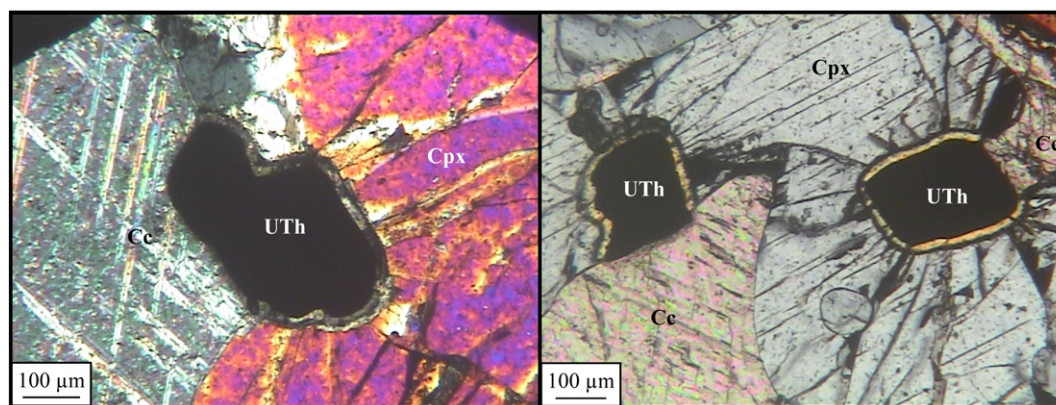
Fig. 1. Optical microscope images showing 3 uranothorianite (UTh) grains included in diopside (Cpx) + calcite (Cc) under crossed polar light. Note the associated structures due to irradiation from α decay of U and Th: (1) cracks, visible only in diopside, radiating from uranothorianite; (2) a diffuse optical halo at calcite–uranothorianite interface; and (3) a wide (~20–30 μm) "reaction zone" along diopside–uranothorianite interface.

2000; Burakov et al., 2002); (4) study of old naturally radioactive minerals in various geological contexts by using various analytical methods like IR (Zhang and Salje, 2001), EXAFS (Farges and Calas, 1991; Harfouche et al., 2005), Raman (Nasdala et al., 1995), RMN (Farnan et al., 2003), RPE (Balan et al., 2005), and TEM (Black et al., 1984; Lumpkin et al., 1986a; Murakami et al., 1991; Weber et al., 1994). The most studied minerals are those that are either used for U–Th–Pb geochronology or expected to be good candidate for nuclear-waste storage, and many papers have been published on zircon (review in Ewing et al., 2003), monazite (review in Ewing and Wang, 2002; Seydoux-Guillaume et al., 2004), titanite (Vance and Metson, 1985; Hawthorne et al., 1991; Lumpkin et al., 1991; Farges, 1997, Zhang et al., 2002), pyrochlore and zirconolite (Lumpkin et al., 1986b; Lumpkin and Ewing, 1988; Farges et al., 1993; Farges, 1997), apatite (Ouchani et al. 1997), and thorite-group (Lumpkin and Chakoumakos, 1988; Farges and Calas, 1991).

However, radioactive minerals not only irradiate themselves, but also the surrounding non-radioactive minerals. This produces concentric structures called "pleochroic halos" or "radiohalos", very familiar to petrologists, who use them to identify radioactive minerals in metamorphic or plutonic rocks. In contrast to the numerous studies dealing with radiation effects in radioactive minerals themselves, the effect of radiation damages in host minerals are rare. The first time that such halo around mineral inclusions was interpreted as being due to the radioactivity of these inclusions was 100 years ago (Mügge, 1907; Joly, 1907). After that, studies on radiohalos were published between the seventies and the nineties (e.g. Gentry, 1973, 1974; Owen, 1988; Odom and Rink, 1989; Meunier et al., 1990). Recently, only two papers deal with radiohalos: in biotite (Nasdala et al., 2001) and in chlorite and cordierite

(Nasdala et al., 2006). These latter studies demonstrated that radiohalos are created by α particles and correspond only to modification of optical characteristics of the host mineral, the various energies of the α particles explaining the difference in size of the halos. Furthermore, those authors found intensive damage (i.e. amorphous domains visible via TEM) only in cordierite up to a few tens of nanometers away from radioactive inclusions. They interpreted these damaged zones to recoil nuclei. Such amorphous zones at the vicinity of a radioactive mineral has already been observed by using Focused Ion Beam–Transmission Electron Microcopy (FIB–TEM) across monazite–quartz boundaries by Seydoux-Guillaume et al. (2003); in this case, the zone was ~150 nm wide.

However, other consequences of radiation damage have not been evaluated. In rocks, poorly crystallized areas, such as the metamict grains but also the damaged zone around them, are actually zones, which can be used by geological fluids to initiate alteration. Another important effect is swelling produced by radiation damage, which can induce cracks around the enclosing minerals, forming pathways for fluids to penetrate into the rock.

The aim of this study is to investigate, by various electron microscopy techniques, the effect of irradiation in a radioactive mineral (uranothorianite) and in the surrounding minerals (calcite and diopside). The geological consequences of radioactive damage for the non-radioactive host minerals and for the whole-rock itself will be discussed.

2. Sample description

The studied sample (SB540) is a diopside-bearing marble within skarns from the Tranomaro area (Andranomitrohy open pit at 46°33.15′ E, 24°19.97′ S) in South-East Madagascar, metamorphosed under granulitic

Table 1
Compositions (in wt.%) of uranothorianite (UTh), diopside (Cpx), calcite (Cc) and sheet silicate (φ) from Fig. 2A obtained by EMP.

# (Fig. 2A)	Uranothorianite (UTh)					Sheet silicate (φ)				Diopside (Cpx)				Calcite (Cc)
	1	2	12	13	14	3	4	5	6	7	8	9	10	11
Na_2O	0.00	0.00	0.08	0.00	0.00	0.07	0.00	0.00	0.00	0.12	0.22	0.21	0.29	0.00
MgO	0.00	0.00	0.00	0.01	0.00	10.56	14.02	15.50	13.75	13.79	13.72	14.05	13.99	0.66
Al_2O_3	0.00	0.00	0.00	0.00	0.00	19.05	18.42	18.75	19.06	8.22	8.19	8.38	8.35	0.00
SiO_2	0.00	0.39	0.00	0.01	0.00	43.58	39.52	33.68	43.81	48.73	48.70	49.27	48.67	0.04
K_2O	0.10	0.03	0.05	0.04	0.11	0.21	0.10	0.03	0.20	0.00	0.00	0.00	0.00	0.00
CaO	0.19	0.25	0.16	0.11	0.16	2.26	1.87	1.94	2.34	25.03	25.38	25.00	25.07	55.95
TiO_2	0.00	0.00	0.00	0.00	0.00	0.25	0.18	0.09	0.24	0.74	0.72	0.83	0.68	0.00
Cr_2O_3	0.04	0.00	0.07	0.00	0.01	0.00	0.04	0.02	0.00	0.00	0.00	0.00	0.02	0.02
MnO	0.00	0.07	0.07	0.05	0.02	0.13	0.01	0.23	0.10	0.11	0.05	0.00	0.04	0.02
FeO	0.12	0.00	0.00	0.01	0.01	6.28	7.55	14.45	7.25	2.36	2.26	2.23	2.50	0.19
PbO	3.77	3.74	4.10	4.33	3.92	0.06	0.17	0.14	0.00	0.25	0.00	0.00	0.05	0.18
ThO_2	66.37	64.80	66.33	66.12	66.99	0.04	0.68	0.10	0.00	0.03	0.00	0.06	0.08	0.00
UO_2	29.24	28.50	30.27	29.76	28.92	0.10	0.00	0.00	0.00	0.00	0.06	0.00	0.01	0.00
Total	99.83	97.78	101.14	100.44	100.15	82.57	82.56	84.93	86.75	99.38	99.31	100.03	99.75	57.06

EMP operating at 15 kV, 20 nA. Standards are: albite (NaKα), periclase (MgKα), corundum (AlKα), wollastonite (Si and CaKα), sanidine (KKα), perovskite (Ti and MnKα), Cr_2O_3 (CrKα), hematite (FeKα), synthetic Pb-glass (PbMβ), synthetic ThO_2-ceramic (ThMα) and synthetic UO_2-ceramic (UMβ).

conditions (4–5 kbar, 800–850 °C; Rakotondrazafy, 1995; Rakotondrazafy et al., 1996) during the Pan-African orogeny (565–580 Ma, Paquette et al., 1994). In this region, at the western border of the Anosyan Belt, uranothorianite mineralization is common (Moine et al., 1985; Boulvais et al., 1998; Ramambazafy, 1998; Ramambazafy et al., 1998; Boulvais et al., 2000). They occur in skarns formed by metasomatic alteration of calcitic marbles (Moine et al., 1985). Fluid inclusions study shows that fluids are CO_2-rich ($X_{CO_2} \geq 0.8$) and in equilibrium with mineral assemblages (Ramambazafy et al., 1998). The hydrothermal/metasomatic mobility of Th can be explained by transport in F-rich fluids as shown by the widespread occurrence of fluor-phlogopite and fluor-pargasite (Moine et al., 1998; Ramambazafy, 1998).

Minerals are essentially aluminous diopside (Cpx) and calcite (Cc_1) sometimes containing uranothorianite inclusions; but spinel, pargasite, plagioclase, phlogopite and zirconolite may also be present. Optical microscope pictures (Fig. 1) show examples of 3 uranothorianite grains included in diopside + calcite. The uranothorianite grains are systematically associated with structures suggesting that radioactivity significantly modified the host non-radioactive minerals. These include: (1) cracks, visible only in diopside, radiating from uranothorianite; (2) a
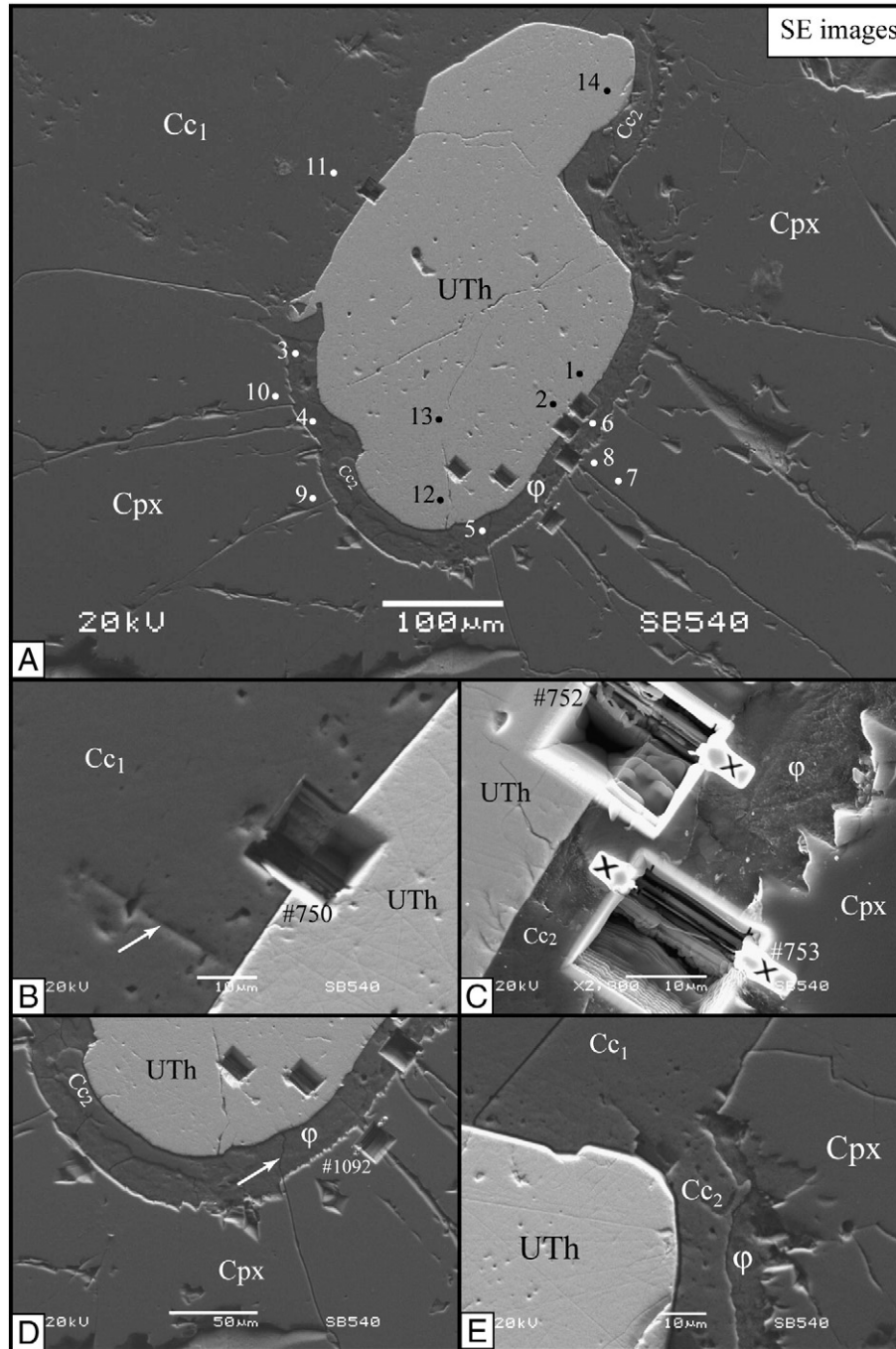
Fig. 2. Scanning Electron Microscope (SEM) images in Secondary Electron (SE) mode from UTh + Cc_1 + Cpx shown in Fig. 1 (left one). A. Note the associated structures due to irradiation from α decay of U and Th: (1) cracks, visible only in diopside, radiating from uranothorianite; (2) a diffuse optical halo at calcite–uranothorianite interface; and (3) a wide (~20–30 µm) "reaction zone" along the diopside–uranothorianite interface. Within this reaction zone, 2 other phases were observed: a secondary calcite (Cc_2) and a clay mineral (φ). 7 FIB holes and Electron Microprobe analyses (see numbers) were also done. B. FIB hole across UTh–Cc_1 boundary (# 750). Note the porosity within Cc_1 and possible remnant of cracks (see arrow). C. Enlargement within the "reaction zone" showing mixture of a secondary calcite (Cc_2) and a low-T clay mineral (φ), and FIB holes done across UTh-φ (# 752) and φ-Cpx (# 753) boundaries. D. Enlargement within the "reaction zone" showing fractures within diopside, with some extended into the reaction zone (arrow), and FIB hole cut across one crack (# 1092). E. Enlargement within the "reaction zone" showing high porosity within Cc_2.

diffuse optical halo at the calcite–uranothorianite interface; and (3), a wide (~20–30 μm) "reaction zone" along the diopside–uranothorianite interface. Only diopside in contact with uranothorianite show these corona; other diopside crystals are pristine indicating these features are due to irradiation coming from α decay of U and Th.

3. Analytical methods

3.1. Scanning Electron Microscope (SEM) and Electron Microprobe (EMP)

SEM images and EDX mapping were performed using the JEOL 6360 equipped with a Sahara detector from PGT at the LMTG-Toulouse.

Quantitative EMP analyses were obtained using the Cameca SX50 at the LMTG-Toulouse operating at 15 kV and 20 nA (Table 1).

3.2. Transmission Electron Microscope (TEM) coupled with Focused Ion Beam (FIB) technique

Since the aim of this study is to investigate the interfaces between grains in thin section, a site-specific preparation method for TEM analysis is needed. This method is called Focused Ion Beam (FIB) and allows cutting site-specific TEM foils, ~15–20 μm by 10–15 μm, and ~100 nm thick (for technical details, see, Overwijk et al., 1993; Young, 1997; Roberts et al, 2001 and Wirth, 2004). TEM samples were milled
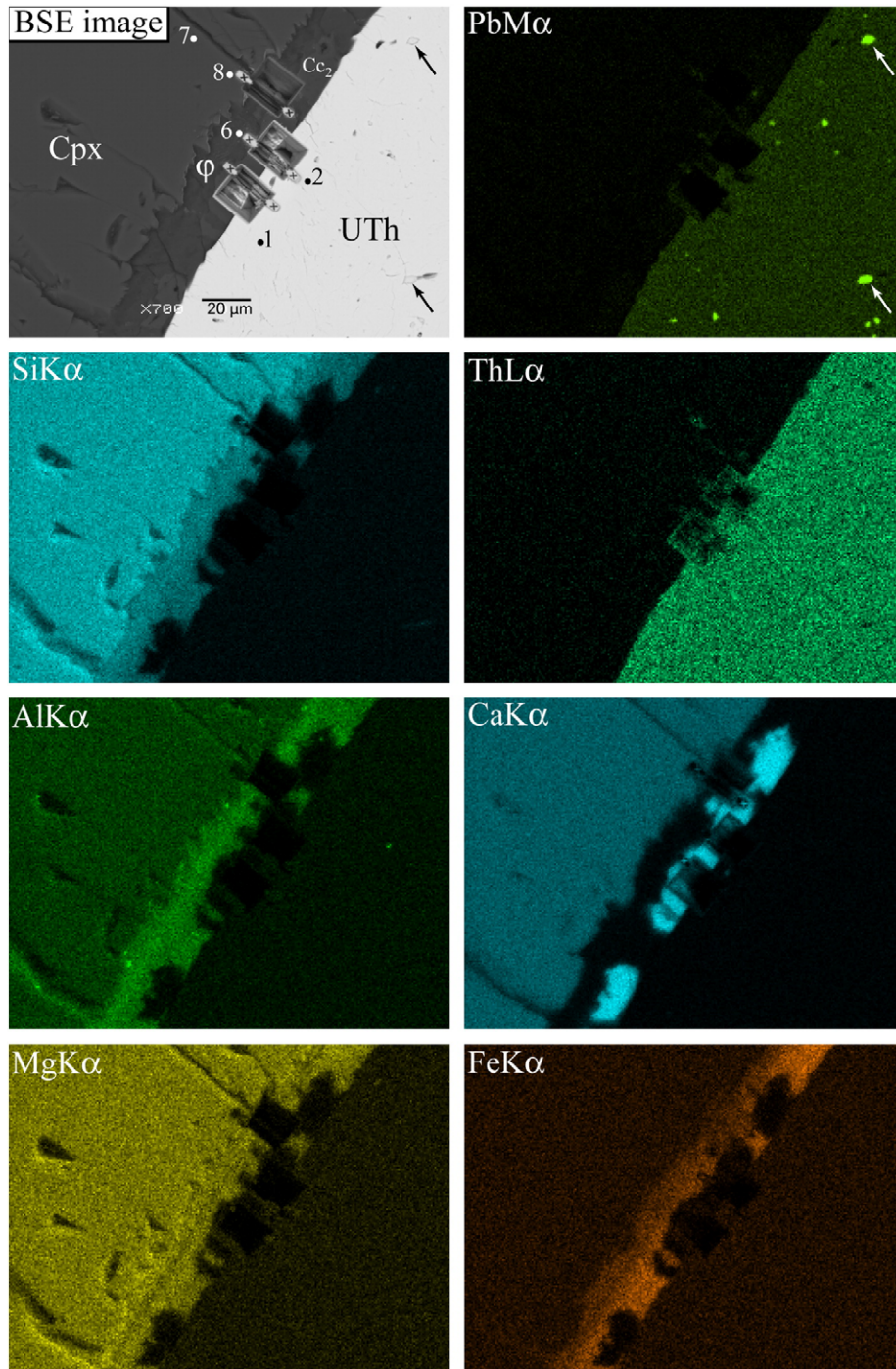
Fig. 3. SEM chemical maps of PbMα, SiKα, ThLα, AlKα, CaKα, MgKα and FeKα of the zone observed in the Back Scattered Electron (BSE) image on the left. Acquisition time was 12.4 sec/image for a total of 140 images and a size of maps of 256×192×16 bits. Note of the high quantity of PbS inclusions within UTh.

by using gallium ions accelerated to 30 keV. The TEM foil is cut perpendicular to the surface of the sample (Fig. 2), providing information with respect to the depth of the specimen. The site-specific specimens were prepared with the FEI FIB200 instrument at the GeoForschungsZentrum (GFZ)-Potsdam.

TEM studies were carried out with the Philips CM200 TEM, operating at 200 keV, equipped with an energy-dispersive X-ray analyzer (EDX) with an ultra-thin window, and a LaB_6 filament as electron source, and the FEI Tecnai™G^2 F20 X-Twin, operating at 200 kV, equipped with a FEG electron source, a high angle annular dark field (HAADF) detector, and an EDAX energy-dispersive X-ray analyzer system; both instruments are installed at the GFZ-Potsdam. Additional selected area diffraction (SAED) patterns were also performed at the TEMSCAN-Toulouse with a Jeol 2010 (200 keV, LaB_6) microscope.

4. Results

4.1. Microscopic study

In agreement with previous studies (Rakotondratsima, 1983; Ramambazafy, 1998), EMP analyses showed that uranothorianite is a solid-solution made of about two-thirds thorianite and third uraninite. The lead content is about 3–4 wt.% PbO. The SEM–EDX map (Fig. 3) shows that uranothorianite contains many Pb-rich inclusions, demonstrated by EMP and TEM to be galena PbS. The chemical ages calculated from U, Th, and Pb content range from 544 to 578 Ma, for four analyses, in agreement with the accepted ages for those rocks, but one analysis gives 931 Ma, due to high Pb content. We think that this analysis was contaminated by a galena inclusion, giving an apparently high Pb content, and then an apparently old age. Clinopyroxene is an Al-rich diopside ($X_{mg} = 0.92$, and 8.3 wt.% Al_2O_3).

The "reaction zone" at diopside–uranothorianite interface (Fig. 2C) consists of a mixture of calcite (secondary calcite, Cc_2), with an Al–Mg–Fe–silicate fibrous phase (φ) (Fig. 2C, D and E). EMP coupled with TEM results (Table 1) demonstrated that it is a low-T phyllosilicate from the smectite group. Secondary calcite is usually located at the inner part of the reaction zone, along uranothorianite, and is always porous, whereas smectite (φ) is located in the outer part along diopside. The diopside-reaction zone grain boundary is locally indented (Fig. 2A, C and D), along the main cleavage direction. The primary calcite–uranothorianite interface is sharp, but calcite in contact with uranothorianite is more or less porous on a ~20 µm layer (Fig. 2B and E), as is secondary calcite in the reaction zone (Fig. 2E).

SEM confirms the presence of cracks radiating around the uranothorianite within clinopyroxene (Fig. 2A and D). Possible remnants of cracks were observed within Cc_1 (arrow Fig. 2B). Some fractures extend into the reaction zone (Fig. 2A and D).

4.2. Nanometric study (FIB/TEM)

TEM samples were prepared using the FIB milling technique across the uranothorianite–primary calcite (#750; Fig. 2B), uranothorianite–secondary calcite (#752) and diopside-reaction zone (#753) interfaces (Fig. 2C); one foil was also cut across a fracture (#1092, Fig. 2D). From selected area diffraction (SAD) patterns (Fig. 4B and C), we can conclude that both primary calcite and uranothorianite are crystalline. The only indication of structural modification in those phases, is mottled diffraction contrast in bright field and dark field images, observed mostly in uranothorianite. In this mineral, diffraction spots are split (Fig. 4C), probably because of PbS inclusions (Fig. 3—PbMα map).

Uranothorianite–primary calcite interface (Figs. 4 and 5): in contrast to what was observed with SEM, there is no direct contact between primary calcite and uranothorianite. Four different zones (A, B, C and D) were identified (Fig. 5). From calcite to uranothorianite, we found: (1) a large (~200–300 nm) amorphous zone (A), enriched in U and Th, but without Si (see U–Th–Si maps in Fig. 5) and enriched in Ca (see EDX spectrum Fig. 5); (2) a chain (B) of very small (~20 nm) ThO_2 crystals free of U (Figs. 4 and 5); (3) another amorphous zone (C), which, in contrast to zone A is enriched in Si; and (4) another zone (D) made of small amorphous Si-rich "bubbles". Many fluid inclusions were observed in the calcite, some of them displaying a "negative crystal" shape (arrow Fig. 4A). *Diopside-reaction zone interface* (Fig. 6): the FIB cut foil shows preferential dissolution of Cpx along cleavages, giving this particular triangular-shaped boundary (Fig. 6A). Within the
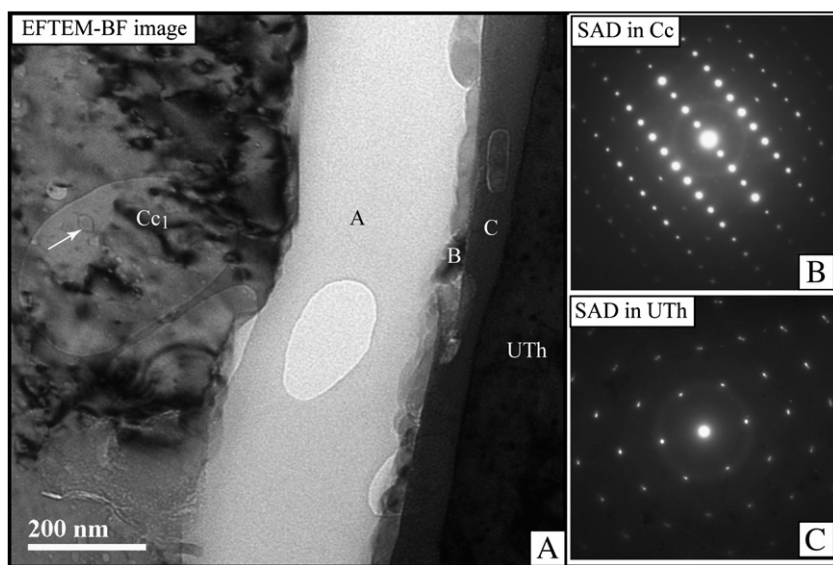
Fig. 4. TEM foil # 750. A. Energy Filtered Transmission Electron Microscope (EFTEM) — Bright Field (BF) image showing presence of an amorphous zone (A) between primary calcite (Cc_1) and UTh. Zone (B) correspond to ThO_2 grains and zone (C) to another amorphous zone (see Fig. 5). Many fluid inclusions were observed in the calcite, some of them displaying a "negative crystal" shape (see arrow). B and C. Selected area diffraction (SAD) patterns in respectively primary calcite and UTh showing that both phases are crystalline. In UTh diffraction spots are split probably because of the presence of PbS inclusions within UTh (arrows in Fig. 3).
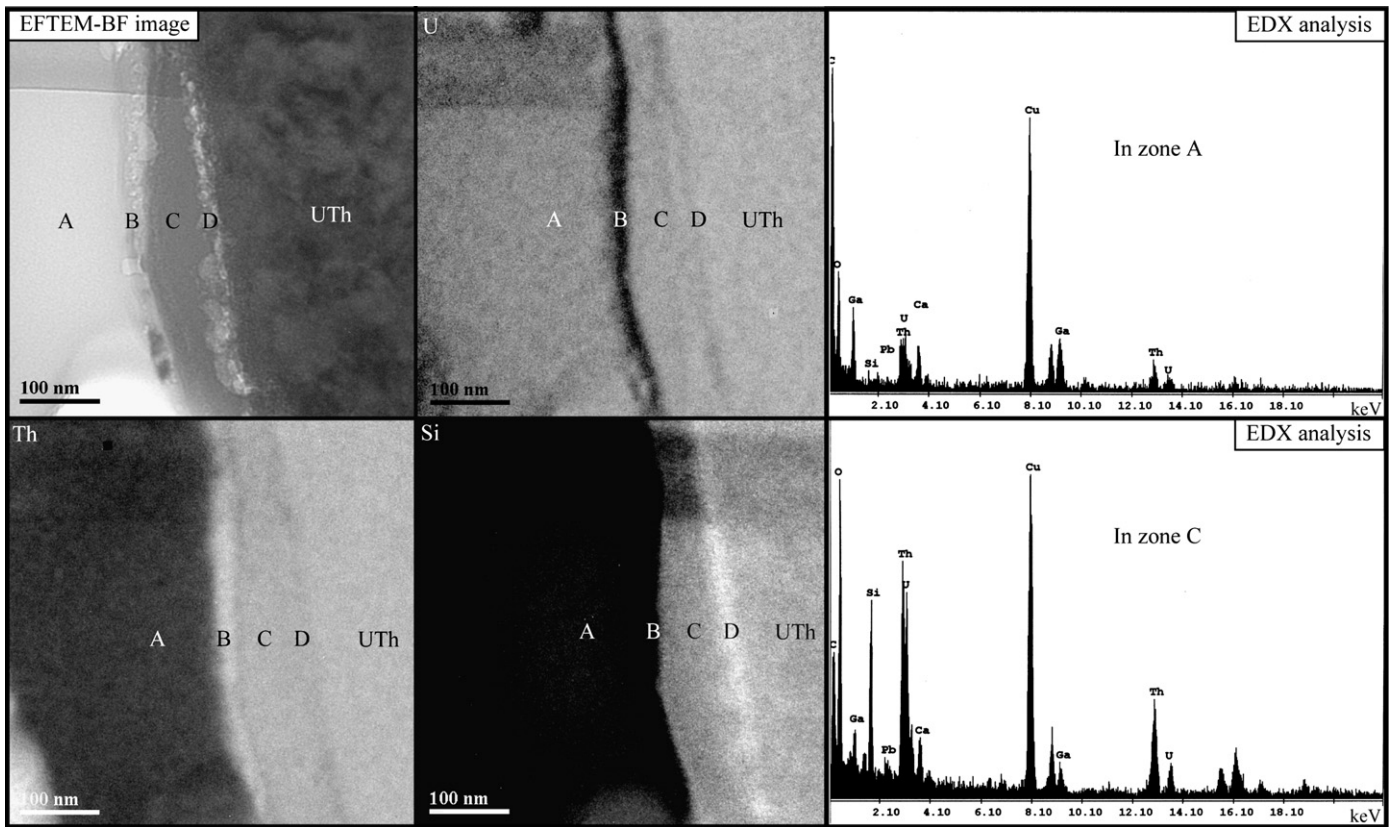
Fig. 5. TEM foil # 750. EFTEM-BF image (on the top on the left), and U, Th, Si-jump ratio maps of the same zone showing from calcite to uranothorianite: (1) a large (~200–300 nm) amorphous zone (A), enriched in U and Th, but without Si (see U, Th and Si maps) and enriched in Ca (see EDX spectrum on the right); (2) a chain (B) of very small (~20 nm) ThO_2 crystals free of U; (3) another amorphous zone (C), which, in contrast to zone A is enriched in Si (see EDX spectrum on the right and Si-map); and (4) another zone (D) made of small amorphous Si-rich "bubbles".

reaction zone an unoriented clay mineral (smectite) was observed, with its typical layer-form (Fig. 6B and C). Many inclusions are present in this zone (arrows on Fig. 6): Pb-rich inclusions as well as and U + Th-rich inclusions.

Uranothorianite–secondary calcite interface (Fig. 7): the organization is similar, but opposite to the uranothorianite–primary calcite interface. An amorphous zone (A) enriched in U, Th and Ca and a chain of ThO_2 crystals (B) parallel to the interface was observed. However the ThO_2 layer is mostly along calcite, and not along uranothorianite, and no Si-rich zone was observed. Secondary calcite contains many fluid inclusions (see arrows in Fig. 7A and C) and U + Th + Pb-rich inclusions (large inclusion Fig. 7A).

Within one crack (Fig. 8): the fracture (~2 μm wide) is filled with a mixture of clay mineral and calcite similar to the reaction zone. It contains also ZrTiCaTh-amorphous phase (Zr), presumably metamict zirconolite, already described in those rocks (Rakotondrazafy et al., 1996). Nano-channels are visible at the interface between diopside and the crack border; the channel is larger (~70 nm compared to ~40 nm) on the upper side (Fig. 8A and B). Bright field (BF) image of the upper channel (Fig. 8B) shows that it is filled with nano-bubbles, i.e. fluid inclusions.

4.3. Summary of petrographic features

The aureole along the diopside–uranothorianite interface is not a pleochroic halo such as described by Nasdala et al. (2001) in biotite or Nasdala et al. (2006) in cordierite. It is a totally transformed zone, filled with material that we could expect to form during low-temperature retrogression of diopside. The transformed zone is rather constant in thickness: 20 to 38 μm, with an average at 27 μm. The transition to pristine diopside is very sharp, but sometime indented. The transformations in primary calcite are less visible but there is actually a porous calcite layer, again 20 to 30 μm thick, although it is there more difficult to estimate. At the nano-scale, the uranothorianite–calcite interfaces are quite complex, with several layers, of various chemical compositions and structural states.

Those observations suggest that primary calcite and diopside located close to uranothorianite has been crystallized at low temperature, as a secondary porous calcite for calcite, and as a mixture of secondary calcite and clay mineral for diopside. The presence of hydrous minerals (smectite) and carbonate (calcite) in reaction zone and in cracks, the presence of Pb-rich inclusions in secondary calcite, the abundance of fluid inclusions in the porous layer in primary calcite, the dissociation of U and Th in the calcite–uranothorianite layer, and the ThO_2 chains along interfaces, are all strong indications that low-temperature crystallization was promoted by a fluid phase.

Surprisingly, truly metamict material is very rare, limited to a narrow (200–300 nm) amorphous layer, along the calcite–uranothorianite interface. However all structures described above are strictly limited to the interface between uranothorianite and other minerals, so must be more or less related to the effect of irradiation. In order to evaluate how irradiation by U and Th could affect the minerals studied above, we carried out a detailed study of irradiation damages using the SRIM/TRIM software.

5. Modeling with SRIM/TRIM

Damage was modeled by using the SRIM/TRIM software package (Ziegler, 2006) which allows simulating the effect a particle in a target, knowing what kind of particle it is, its energy, and the density and chemical compositions of the target. It is based on full-quantum calculations of individual interactions of incident particles with the atoms of the target. For our purpose the interesting outputs are the particle path (in three dimensions), and the vacancies created in the
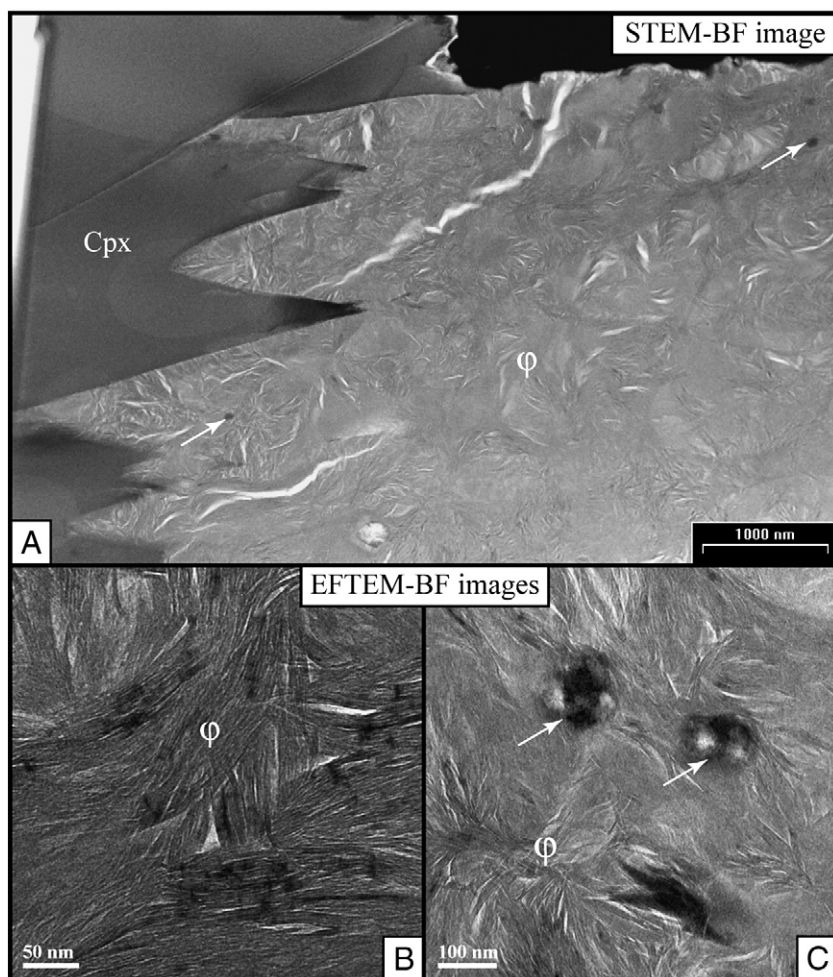
Fig. 6. TEM foil # 753. Scanning Transmission Electron Microscope Bright Field (STEM-BF) image (A) and EFTEM-BF images (B and C) showing preferential dissolution of diopside (Cpx) along cleavages, giving this particular triangular-shaped boundary, an unoriented clay mineral (φ-smectite), with its typical layer-form (B and C), and many Pb-rich as well as U + Th-rich inclusions (arrows in A and C).

target. SRIM/TRIM always assumes that the target is amorphous and isotropic.

5.1. Irradiation by U and Th chains

Irradiation by U and Th is done by all the radioelements of the ^{235}U, ^{238}U, and ^{232}Th decay chains which combine α and β decays to reach the final stable nuclei: ^{207}Pb, ^{206}Pb and ^{208}Pb respectively. We will neglect the β decay which produces no major damage, and we will neglect also α decays of minor branched radioactivity. During α decay, two particles are created: the α particle itself, which is a ^4He nucleus, and the recoil nucleus, which is actually the nucleus of the daughter element, belonging to elements from U to Tl. The total energy involved during an α decay is few MeV, distributed unevenly between the two particles (about 100 keV for the recoil, and the rest for the α). Then each α decay produces a slow, heavy nucleus (recoil), and a light, fast particle (α). Another source of damage in radioactive minerals is the spontaneous fission of ^{238}U. It is a rare event (0.00005% of the ^{238}U decay) but the energy involved is about 200 MeV, and it produces two fissions nuclei with atomic number around 100 and 140 respectively. The energies of the particles of the three decay chains are summarized in Table 2. For α particles, it ranges from 4 to 8.8 MeV and for recoil for from 70 to 170 keV.

Using SRIM we calculated the effect of α and recoil particles of the three decay chains, in diopside, calcite and uranothorianite, as well as the effect of two typical fission products ^{90}Y and ^{140}Ce. Usually 1000

particles are calculated to obtain good statistics. Two key outputs are presented in Table 2: the average distance reached by the particle, and the number of vacancies created. To illustrate the effect of α and recoil particles in minerals, the vacancy distributions for the $^{214}Po \Rightarrow {}^{210}Pb$ decay in diopside (α:7.69 MeV; recoil:146 keV), are presented in Fig. 9. For other decays or other minerals, the amount of vacancies and the distances are different, but the shapes are similar. The effects of α particles and recoil nuclei are fundamentally different. The α particles are penetratives (12–38 µm in diopside, 14 to 45 µm in calcite) and produce 220 to 270 vacancies in diopside and 170–200 vacancies in calcite. The recoil nuclei are 1000 times less penetrative (27–45 nm in diopside, 32–55 nm in calcite) but 10 times more destructive (1200–2500 vacancies in diopside, 940–2030 vacancies in calcite). The fast α particle produces vacancies only at the end of its displacement, when it has been slowed down enough by ionization to interact with target nuclei. The slow recoil nucleus creates vacancies all along its trajectory. In three dimensions, the trajectory of a series of α particles has the shape of a cone, while it is pear-shaped for the recoils. The maximum distance reached by an α particle is very close to the average distance, whereas it is about twice as long for recoil nuclei. Fundamentally the length of the trajectory increases with increasing energy, and decreases with increasing density of the target. In uranothorianite the length of the trajectories are about 9 to 30 µm for α particles, so only the outer part of the uranothorianite irradiates the surrounding minerals.
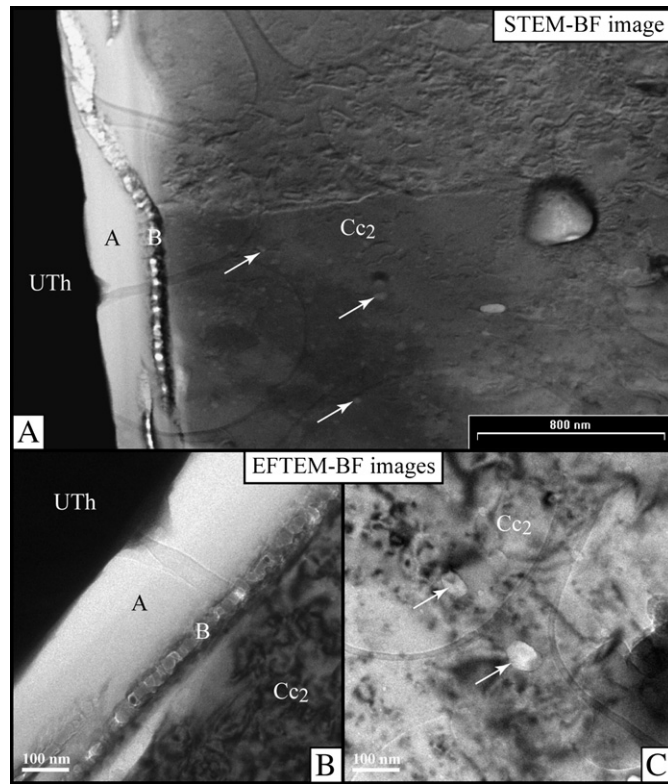
Fig. 7. TEM foil # 752. STEM-BF image (A) and EFTEM-BF images (B and C) showing a similar organization but reversed from the uranothorianite–Cc_1 interface: an amorphous zone (A) enriched in U, Th and Ca and a chain of ThO_2 crystals (B) parallel to the interface (see also image B). Secondary calcite (Cc_2) contains many fluid inclusions (see arrows in A and C) and U + Th + Pb-rich inclusions (large inclusion on the right).

5.2. Geometry

SRIM/TRIM simulates only the effect of a particle thrown into a target along a single direction. In the present study we are studying the effect of a layer of radioactive material (the outer part of the uranothorianite grain) into a non-radioactive material (diopside and calcite). The vacancy distribution calculated by SRIM/TRIM must then be corrected. First, because radioactive decay emits particles in random directions and not along a single path, and second, because the emitting volume is a layer and not a point. The main output of SRIM/TRIM is the linear density
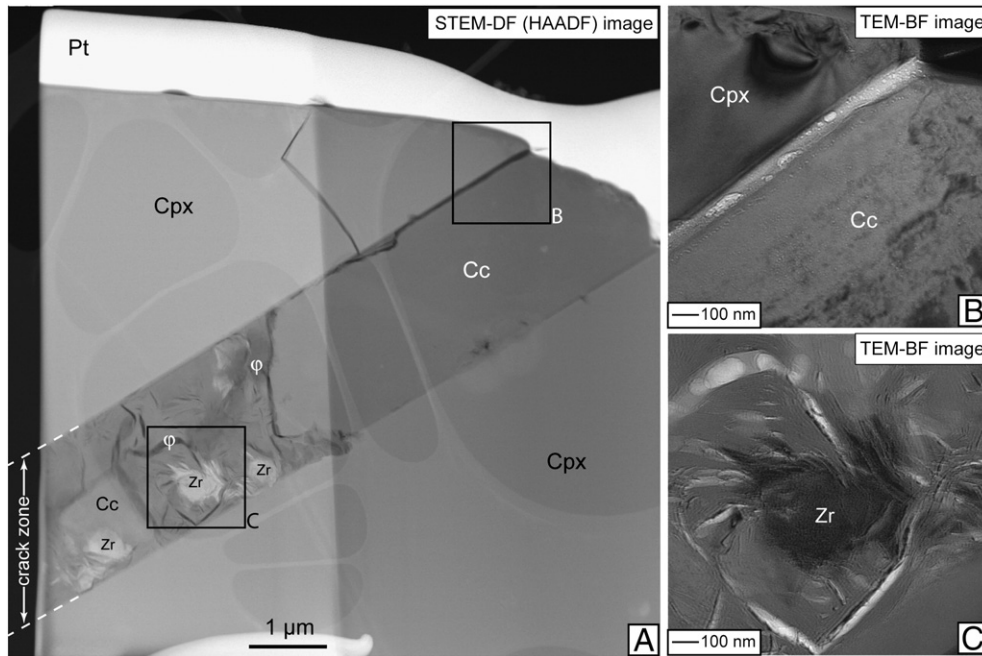
Fig. 8. TEM foil # 1092. STEM — Dark Field (DF) image (A) done with high angle annular dark field (HAADF) detector and TEM-BF images (B and C) showing TEM foil cut across one fracture within Cpx (see Fig. 2D). The fracture (~2 μm wide) is filled with a mixture of clay mineral (φ), calcite (Cc), and a ZrTiCaTh-amorphous phase (Zr), presumably metamict zirconolite (A). Nano-channels, filled with nano-bubbles (fluid inclusions) are visible at the interface between Cpx and the crack border (B); the channel is larger (~70 nm compared to ~40 nm) on the upper side (A and B).

Table 2
Summary of the results of TRIM/SRIM calculations.

	E (MeV)	Alpha particles						E (keV)	Recoil nuclei					
		Diopside		Calcite		Uranothorianite			Diopside		Calcite		Uranothorianite	
		dist	dam	dist	dam	dist	dam		dist	dam	dist	dam	dist	dam
^{238}U														
$^{238}U \Rightarrow ^{234}U$	4.20	12.3	228	14.6	172	9.7	184	71	27	1231	33	983	16	971
$^{234}U \Rightarrow ^{230}Th$	4.78	14.8	225	17.5	186	11.5	190	83	29	1414	36	1129	16	1124
$^{230}Th \Rightarrow ^{226}Ra$	4.69	14.4	221	17.1	178	11.2	198	83	29	1381	36	1117	17	1113
$^{226}Ra \Rightarrow ^{222}Rn$	4.79	14.7	224	17.5	179	11.5	190	86	29	1447	36	1145	18	1141
$^{222}Rn \Rightarrow ^{218}Po$	5.49	18.0	238	21.4	184	14.0	203	90	31	1485	41	1315	19	1312
$^{218}Po \Rightarrow ^{214}Pb$	6.00	20.5	236	24.4	193	15.9	206	112	35	1826	43	1456	22	1467
$^{214}Po \Rightarrow ^{210}Pb$	7.69	30.0	251	35.7	197	22.9	224	146	42	2300	53	1830	24	1836
$^{210}Po \Rightarrow ^{206}Pb$	5.31	17.1	236	20.4	185	17.1	209	103	34	1694	42	1357	20	1341
^{232}Th														
$^{232}Th \Rightarrow ^{228}Ra$	4.01	11.8	219	14.0	173	9.0	136	69	27	1191	32	937	15	927
$^{228}Th \Rightarrow ^{224}Ra$	5.42	18.1	232	21.4	186	13.7	194	95	31	1577	38	1247	19	1224
$^{224}Ra \Rightarrow ^{220}Rn$	5.69	19.4	231	23.0	177	14.6	210	102	32	1647	40	1329	19	1310
$^{220}Rn \Rightarrow ^{216}Po$	6.29	22.5	233	26.7	189	16.9	203	114	35	1848	43	1459	21	1443
$^{216}Po \Rightarrow ^{212}Pb$	6.78	25.2	252	29.9	193	18.8	213	126	38	2032	46	1607	23	1595
$^{212}Bi \Rightarrow ^{208}Tl$ (36%)	6.09	21.5	231	25.5	194	16.1	203	115	34	1863	43	1470	21	1450
$^{212}Po \Rightarrow ^{208}Pb$ (64%)	8.79	37.8	268	44.7	201	27.7	225	166	45	2592	55	2029	44	2038
^{235}U														
$^{235}U \Rightarrow ^{231}Th$	4.69	14.3	221	17.1	178	10.9	192	81	29	1386	35	1095	16	1057
$^{231}Pa \Rightarrow ^{227}Ac$	5.06	16.0	231	19.0	181	12.1	192	89	30	1497	36	1194	18	1179
$^{227}Th \Rightarrow ^{223}Ra$	6.04	20.8	239	24.7	190	15.6	206	108	34	1754	42	1406	21	1382
$^{223}Ra \Rightarrow ^{219}Rn$	5.87	19.9	235	23.7	180	15.0	199	107	35	1742	42	1400	21	1376
$^{219}Rn \Rightarrow ^{215}Po$	6.82	24.9	243	29.6	191	18.6	214	127	37	2035	47	1623	24	1597
$^{215}Po \Rightarrow ^{211}Pb$	7.39	28.2	245	33.5	197	21.0	204	140	41	2244	50	1785	26	1750
$^{211}Bi \Rightarrow ^{207}Tl$	6.62	23.8	241	28.3	185	17.8	207	128	38	2055	47	1634	26	1604
Fission														
^{90}Y (100 MeV)		15.8 µm 39000 vacancies/ion							9.10 µm 43500 vacancies/ion					
^{140}Ce (100 MeV)		17.5 µm 81000 vacancies/ion							8.50 µm 95700 vacancies/ion					

E: energy of the particle, in MeV (alpha) or in keV (recoil); dist: average distance done by the particle in µm (alpha) or in nm (recoil); dam: damage in vacancies/ion.

of vacancies created by a particle, expressed in vacancy/ion/Å, hereafter named VAC$(r)_{\text{linear}}$ with r being the distance (radius). A series of N particles, along a small distance dr situated at a distance r of the emitting volume creates a number of vacancies $N \cdot$ VAC$(r)_{\text{linear}} \cdot$ dr. In three dimensions, because of the random direction of the emission, the same amount of vacancies is diluted in a fraction of sphere $4\pi r^2 \cdot$ dr. Therefore the vacancy density per ion around an emitting center is:

$$VAC(r)_{\text{sphere}} = \frac{VAC(r)_{\text{linear}}}{4\pi r^2} \qquad (1)$$

This expression is fundamentally the same as in Nasdala et al. (2001), but calculated by differentiation.

As shown in the first part of this paper the thickness of the damaged area (20–30 µm) is small compared to the length of the uranothorianite–diopside/calcite interface (few hundreds of µm). Therefore we will consider the irradiation geometry to be a plane separating a radioactive domain from a non-radioactive domain. Each volume of the irradiated medium situated at a distance L from the interface will receive VAC$(r)_{\text{sphere}}$ damages from all the particles emitted from the radioactive medium and situated at a distance r. The volume of radioactive medium situated at a distance r is:

$$V\text{rad} = \Omega \cdot r^2 \cdot dr \qquad (2)$$

with Ω the solid angle of the cone defined by r and L, which is given by

$$\Omega = 2\pi \left(1 - \frac{L}{r}\right). \qquad (3)$$

Combining Eqs. (1)–(3) and summing over the whole radioactive volume, we obtain the density of vacancies created at a distance L of the radioactive half-space:

$$VAC(r)_{\text{plane}} = \int_{L}^{\infty} \frac{1}{2} \cdot VAC(r)_{\text{linear}} \cdot \left(1 - \frac{L}{r}\right) \cdot dr. \qquad (4)$$

Since we do not have an analytical expression for VAC$(r)_{\text{linear}}$, this can only by estimated numerically from the output of SRIM/TRIM. The calculation of the exact expression would require calculating each VAC$(r)_{\text{linear}}$ function for all L and all particles. In order to maintain the calculation time reasonable we decided, for each particle and each target, to use only the VAC$(r)_{\text{linear}}$ function calculated for the target mineral. The consequences of this approximation will be discussed later.

5.3. The time scale

The petrological study showed that the altered aureole was formed by recrystallization of the target minerals, calcite or diopside. To estimate the amount of damage that the target had experienced when recrystallization occurred, we should know the time at which damage started, assumed to be the age of the rock formation (550 Ma), and the time at which alteration and recrystallization occurred, which is unknown. This initial damage at recrystallization is not zero because some lead, presumably radiogenic has been found in the altered aureole, but it can be from few millions to few hundredths of millions years. This is a major uncertainty, which affect the amount of damage and the relative proportion of damages due to the ^{235}U, ^{238}U and ^{232}Th chains. However neither the size of the damaged area, which depends only on the nature of the target and the particles energy, nor the shape of the vacancy distribution, which depends mainly on the shape of
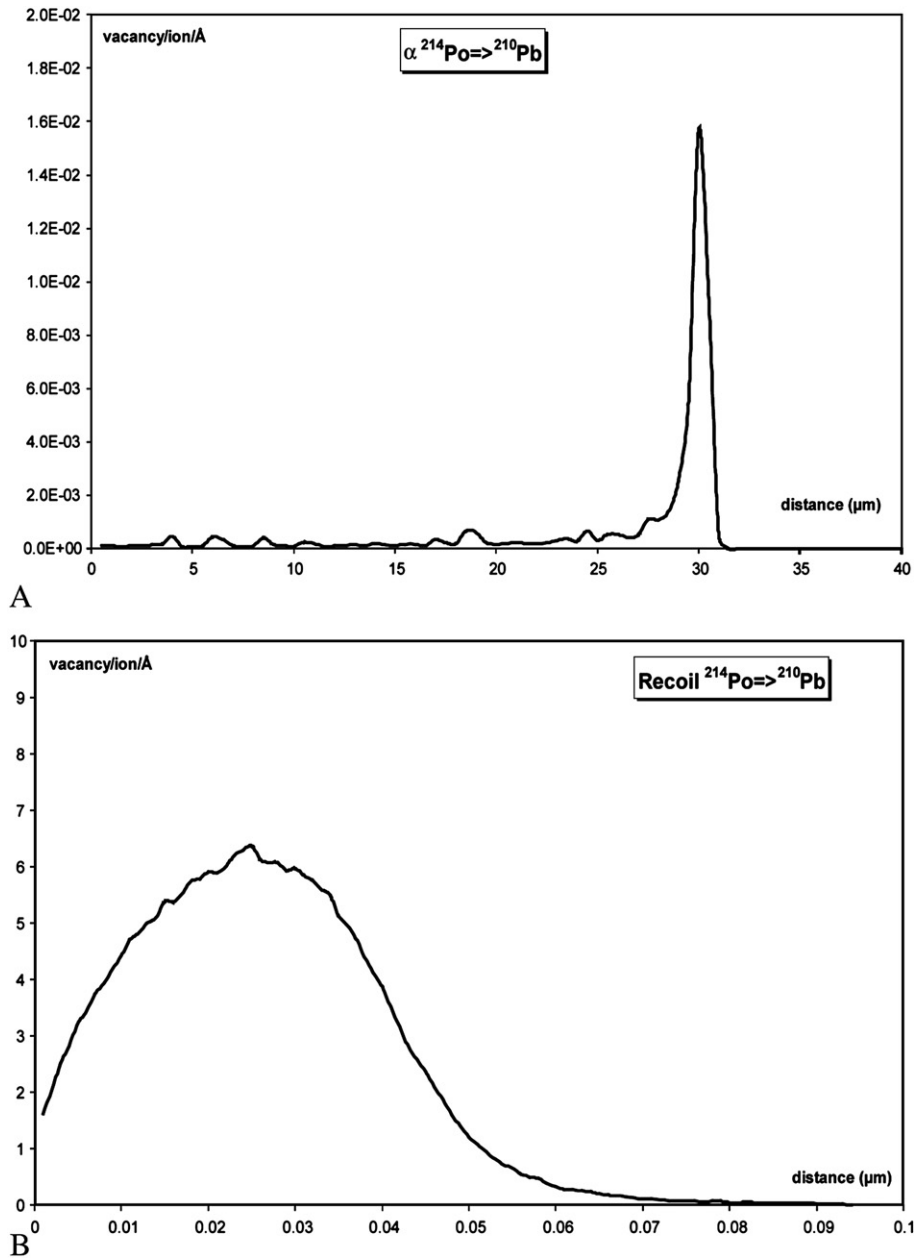
Fig. 9. Projection of the vacancy distribution created by a 7.69 MeV α particle (A) and the corresponding recoil (B) nuclei (^{210}Pb at 146 keV) in diopside. The fast α particle produces vacancies only at the end of its displacement, when it has been slowed down enough by ionization to interact with target nuclei. The slow recoil nucleus creates vacancies all along its trajectory. Note that vertical and horizontal scales are very different in the two figures.

individual particle damaging and of the geometrical corrections, are affected. All the calculations have been carried out assuming 550 Ma as the irradiation time. As a result of this major uncertainty, we made no attempt to estimate dpa (displacements per atom) from the number of vacancies in target minerals.

5.4. Results

Uranothorianite has been auto-irradiated since its formation. It is possible to calculate the number of vacancies directly from the average damage in Table 2, integrated over 550 Ma, and converted it in dpa (displacement per atom). The calculated average of 240 dpa over 550 Ma, when compared to the dose necessary to completely amorphized thorite (ThSiO$_4$), ~0.20 dpa at room temperature (Meldrum et al., 1999), suggests that the uranothorianite should be completely amorphous. However, because electron diffraction patterns (SAD–

Fig. 4) demonstrate that it is crystalline, uranothorianite must self-anneal by some processes. As a comparison, amorphization of UO$_2$ seems impossible, because of the highly rapid recombination of the bonding; for an irradiation dose equivalent to 25 dpa at ~170 °C, UO$_2$ is still crystalline (Matzke and Turos, 1992; Matzke and Wang, 1996).

Results for diopside and calcite are presented in Figs. 10 and 11. Spontaneous fission of ^{238}U is such rare event that it can be neglected. The shapes of the curves, representing the damage due to α particles as a function of distance from uranothorianite are similar. Most damage is accumulated at short distances (about 15 μm in diopside and 17 μm in calcite). The more distant part corresponds to the area damaged only by the more energetic particles emitted close to the uranothorianite surface. The total damaged area is then about 35 μm wide in calcite and 30 μm in diopside. Recoils nuclei create 1000 times more damage than α particles, with a very steep decrease for a damaged zone of 60 nm in calcite and 50 nm in diopside.

The thickness of the damaged area calculated for α in diopside is similar to the width of the recrystallized area observed in thin section. The thickness of the porous calcite layer around along the primary calcite–thorianite interface is more difficult to estimate but is also similar to the size of the area damaged by α as calculated above. However the characteristic distances calculated for the damage of recoil nuclei (50 to 60 nm) are far away from the size of the totally amorphous layer seen at the calcite–uranothorianite interface (150–250 nm).

5.5. Effect of wandering recoils

Modeling the effect of recoil nuclei by a succession of individual ions projected from uranothorianite into the target is, actually, a poor representation of the real process occurring during the radioactive decay of a chain. In decay chains the recoil nucleus is the next radioactive element. During radioactive decay, the recoil moves of few tens of nm, in a random direction. Therefore, there is a possibility, for decay occurring close to the uranothorianite surface, that after decay the recoil is indeed located out of the uranothorianite. Then next decay will occur inside the diopside (or calcite), and the new recoil

will move again, in a random direction. For damages created by α this effect can be neglected, because the path of α is much longer than the possible displacement of the recoil, but for the recoil itself, the damaged area can be significantly enlarged by the "wandering recoil effect": a series of recoils that would move always in the same direction, although very unlikely, can ends few hundredths of nm inside diopside (or calcite). In order to quantitatively estimate this effect we simulated this effect by the following procedure: (1) for each decay, a random direction is chosen; (2) the average damage is distributed along the path, as calculated by SRIM/TRIM; (3) the recoil (daughter) nucleus is displaced in that direction, at the average distance shown in Table 2; (4) the next decay in the chain is processed from this position, as described in (1)–(2)–(3). For each chain and for both diopside and calcite we simulated 1000 decay chains. At the end of the calculation, the radial distribution of the damages is calculated. Strictly, this procedure only simulates a decay chain initiated exactly at the interface. Again, because we do not know the time scale, but only the shape of the curves, only the characteristics distances have real meanings in this simulation. The results are presented in Fig. 12. The main result is that the thickness of the area damaged by the recoils is approximately multiplied by 3 because of the
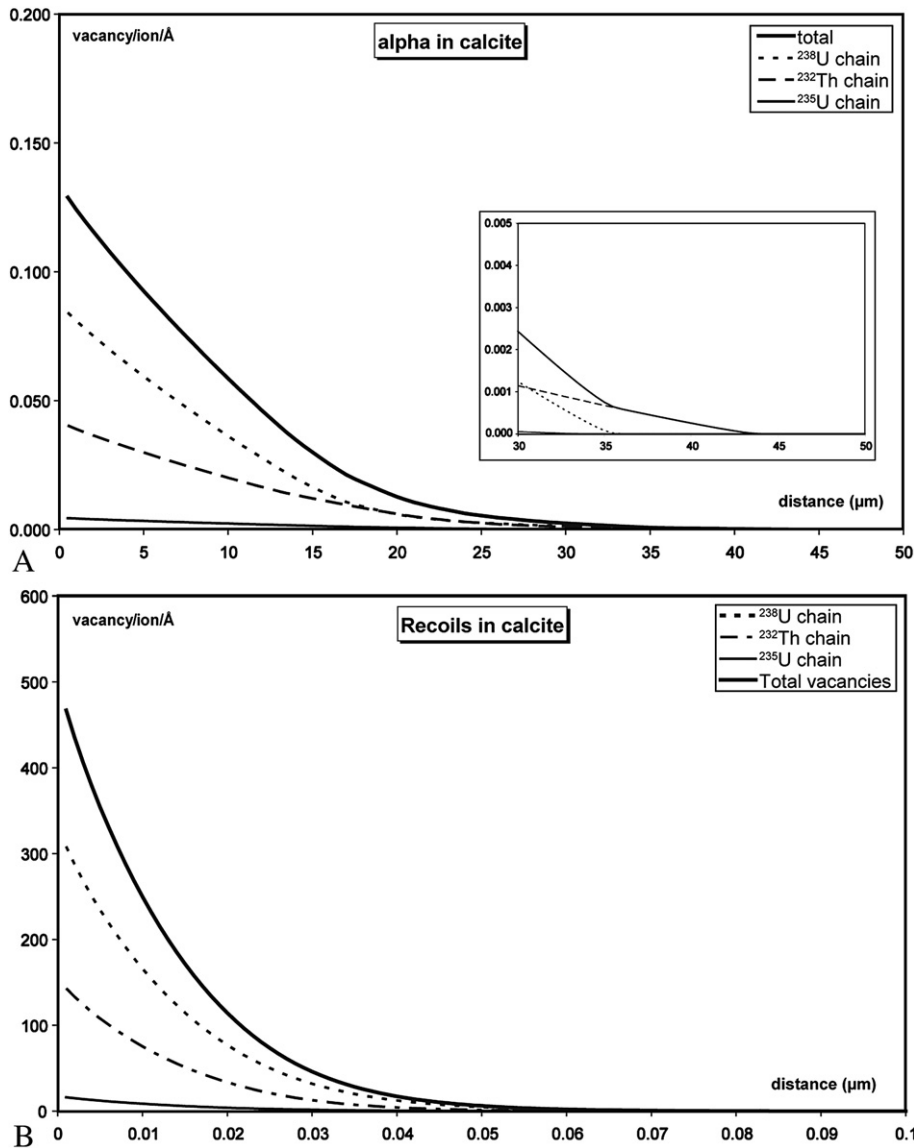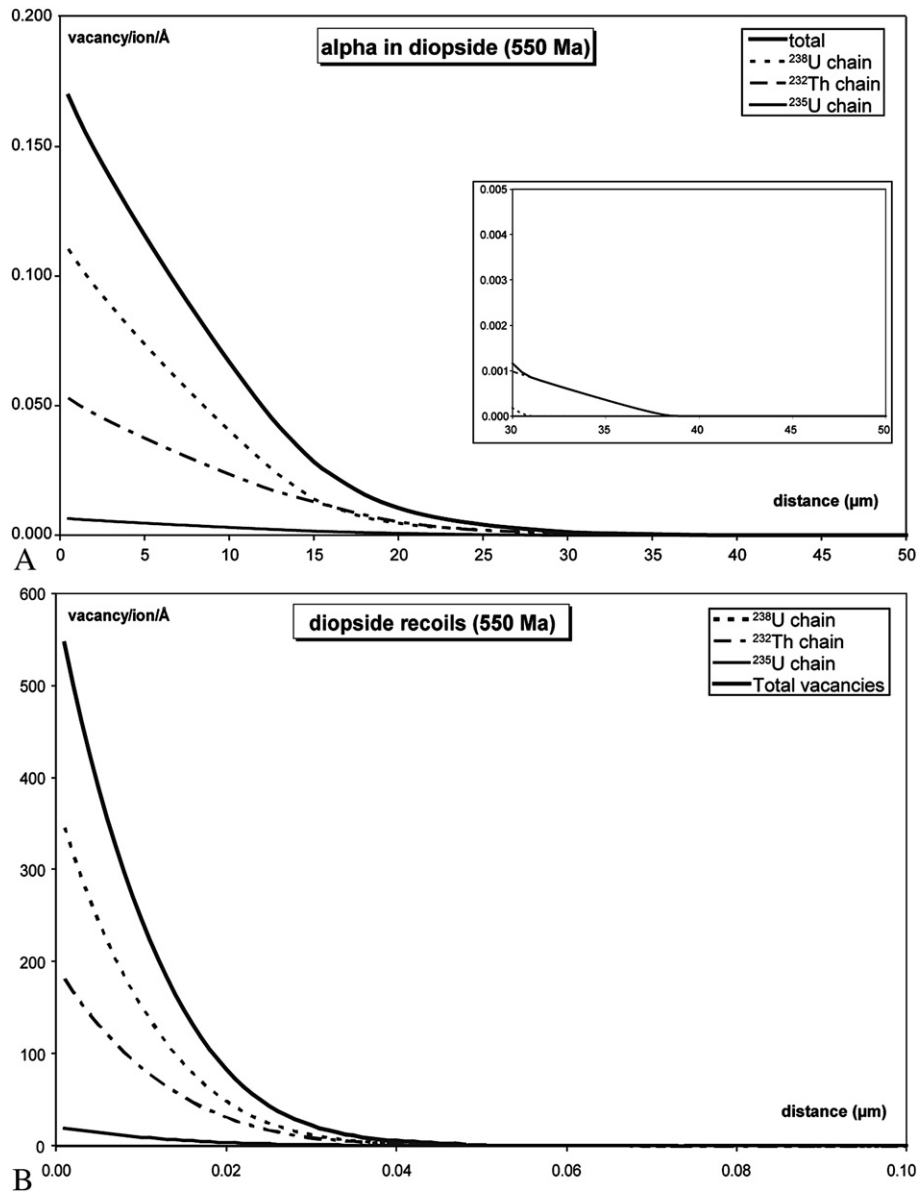

Fig. 10. Spatial distribution of the vacancies created in calcite by α particles (A) and recoil nuclei (B) emitted by uranothorianite. The calculation includes all particles from the three decay chains, integrated for 550 Ma. It assumes that uranothorianite is a semi-infinite emitting medium irradiating a semi-infinite calcite half-space, separated by a plane. Note that vertical and horizontal scales are very different in the two figures.

Fig. 11. Spatial distribution of the vacancies created in diopside by α particles (A) and recoil nuclei (B) emitted by uranothorianite. The calculation includes all particles from the three decay chains, integrated for 550 Ma. It assumes that uranothorianite is a semi-infinite emitting medium irradiating a semi-infinite diopside half-space, separated by a plane. Note that vertical and horizontal scales are very different in the two figures.

"wandering recoil effect". With this correction, the size of the area damaged by recoil nuclei in calcite is in rather good agreement with the thickness of the totally amorphous layer at the calcite–uranothorianite interface (Figs. 4 and 7).

6. Interpretation and discussion

6.1. A reasonable history of radiohalos in Tranomaro skarns

From petrographical study and damage modeling, the evolution of the rock can be reconstructed as follows. The initial rock is a high-temperature marble, mainly made of aluminous diopside and primary calcite, with some large uranothorianite grains. As soon as the latter is formed, radioactive decays start, with three consequences: (1) radiogenic Pb accumulates in uranothorianite; (2) radiation damage accumulates in uranothorianite and in the contiguous minerals; and (3) the uranothorianite grains swells because of radiation damage. For uranothorianite similar to the minerals studied here, Evron et al. (1994) estimated a macroscopic volume expansion of ~1.5%. With

increasing time, swelling creates radial cracks in diopside and calcite, and radiation damage accumulates and weakens calcite and diopside around uranothorianite. A heavily damaged (amorphous) thin layer is created along the interface by the recoils, and a partially or totally damaged layer, 20–40 μm is created by α. Since no Helium bubbles was observed within uranothorianite by TEM, it is supposed that radiogenic Helium diffused out of the crystal through the cracks. After some time, a low-temperature fluid infiltrates through the rock, using the cracks and the weak interfaces as preferential pathways. The damaged part of diopside is retrogressed as a mixture of clay and secondary calcite. The damaged part of primary calcite recrystallized as a secondary porous calcite layer. At this stage, cracks in calcite are healed, whereas, cracks in diopside are partially filled by various secondary material (Fig. 8; calcite, zirconolite, clay mineral). Uranothorianite is also affected by fluids, as shown by the presence of Pb, U, and Th in the reaction zones (Fig. 6) and in the amorphous layers A and C (Figs. 4 and 5), and the presence of ThO_2 chains (Figs. 4, 5 and 7). However the fact that the chemical ages are in good agreement with the age of the rock indicates that this mineral is not deeply penetrated
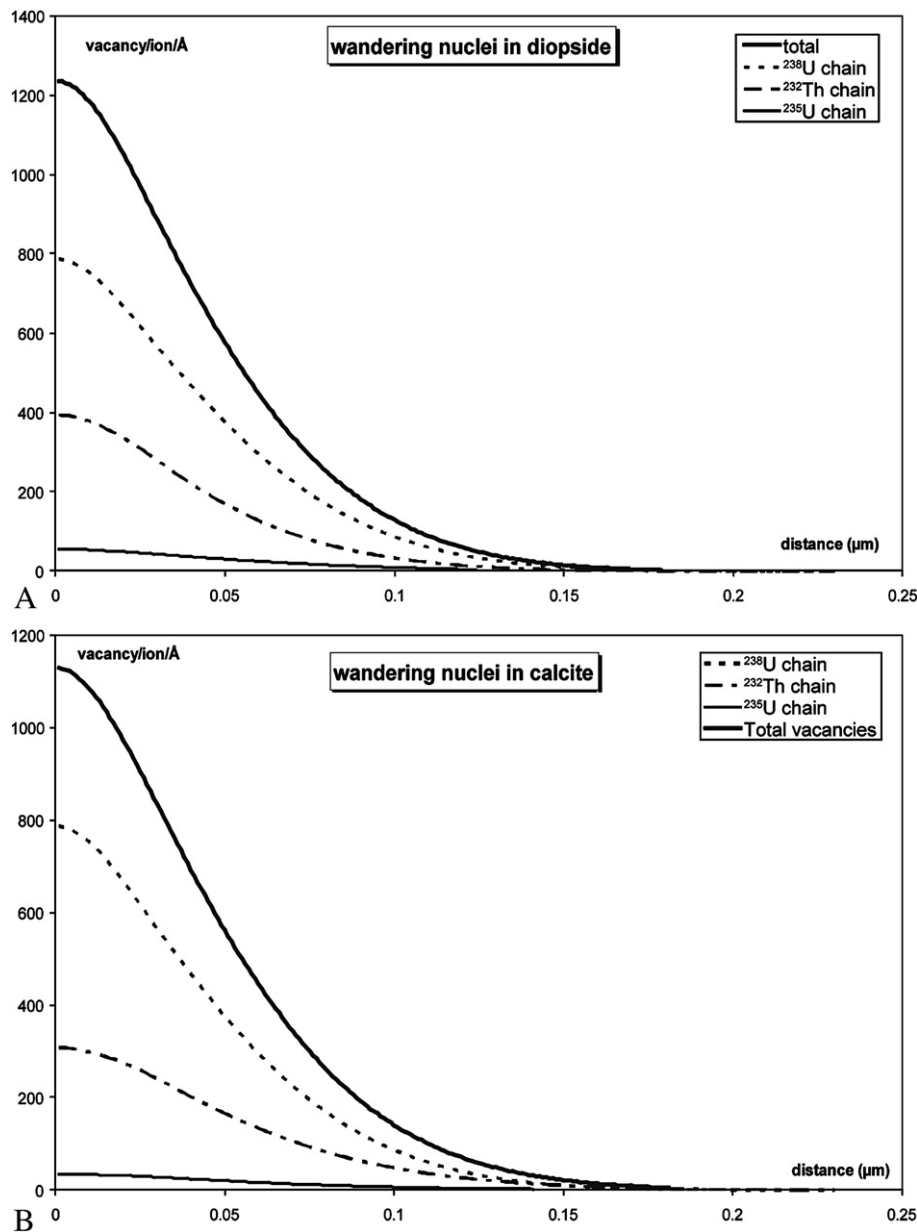
Fig. 12. Spatial distribution of the vacancies created in diopside (A) and calcite (B) by wandering nuclei. The model simulates the random trajectories of recoil nuclei during the successive decays in the three decay chains, and estimates, via TRIM/SRIM simulation the vacancies created along the path. The integration time is 550 Ma. Those diagrams should be compared to Figs. 10 and 11(B).

by fluids. During fluid infiltration, some elements are partially redistributed, including elements which are not obviously present in the thin section such as Zr. After this hydrothermal episode, the newly formed phases are again affected by radioactive damage.

The exact significance of the features observed along the uranothorianite and calcite is at this stage not totally explained. However the B zone, a chain of ThO$_2$ grains, suggest an *in-situ* reprecipitation of ThO$_2$ during partial dissolution of uranothorianite, as it is commonly observed in experiments with ThO$_2$ (Seydoux-Guillaume et al., 2002; Heisbourg et al., 2003; Heisbourg et al., 2004).

6.2. Some properties of uraninite, calcite, and diopside relative to radiation damages

The observations made on this sample support several hypotheses on the behavior of calcite, diopside and uranothorianite under irradiation. Uranothorianite is remarkably resistant to irradiation damage. This is not unexpected, since uraninite, which is isostructural with uranothorianite remains crystalline (Evron et al. 1994; Janeczek et al. 1996). By contrast, a thorium silicate (ThSiO$_4$) that accumulated approximately the same dose as the uranothorianite studied here (~5 × 10^{20} α/g) is completely amorphous (Seydoux-Guillaume et al., 2007). This observation is consistent with higher resistance to amorphization by radiation damage (or greater ability to self-anneal) in minerals for which the long-range ionic forces dominates over the short-range covalent forces (Trachenko, 2004), as in the case for uranothorianite when compared to thorite.

Contrary to uranothorianite, diopside seems to be highly sensible to radiation damage. The average size of the retrogressed zone is 27 μm. At this distance the damage is only 2% of the maximum damage created by the α at the contact with uranothorianite. For 550 Ma of irradiation, this would correspond to 0.0014 dpa, so it means that the resistance of diopside relative to low-temperature fluids is modified even if about 1/1000 atoms are displaced. We should recall that

550 Ma is the maximum for the irradiation time since it assumes that retrogression occurred at the present time.

The limit between pristine diopside and the retrogressed area is very sharp; there is no intermediate zone in which diopside would be partly retrogressed. This suggests that there is a threshold in the sensitivity of damaged diopside to low temperature fluid. Below a certain value of damage the diopside behaves as an undamaged diopside, and is not affected by alteration. We should recall that diopside is a common mineral in heavy minerals concentrates in river, so it is not normally destroyed by low-T fluids.

In calcite the porous layer, which can be assumed to be the equivalent of the retrogressed zone in diopside, is ~10 to 15 μm wide, as estimated from Fig. 2. At this distance damage is 45 to 25% of the maximum (550 Ma) α damage, for 0.013 to 0.0055 dpa. Calcite seems then more resistant to irradiation damage than diopside, probably due to the type of interatomic forces in that structure (Trachenko, 2004). It is important to remember, that diopside crystals that are not in contact with uranothorianite in the rest of the rock are pristine. This demonstrates that irradiation is responsible for the destabilization of diopside by fluids. However, calcite directly in contact with uranothorianite (see presence of Ca within amorphous zone A (Figs. 4A and 5) is amorphous, showing the strong effect of "continuous irradiation by wandering recoil". It should be also noted that calcite is always crystalline, even at the contact with uranothorianite where the damage rate can be up to 0.055 dpa.

Outside the modified area around uranothorianite, the rock is very fresh; the only indication of the low-T fluid infiltration is secondary material along the diopside–uranothorianite interfaces and, at nano-scale, in swelling structures, i.e. cracks (Fig. 8). This definitely shows that uranothorianite grains create weak zones in the rock, by destroying the surrounding minerals, and by creating swelling cracks.

The thickness of the retrogressed area at the diopside–uranothorianite interface is approximately constant all around the thin section. It means that the effect of irradiation damage in diopside does not depend on the orientation of the diopside crystals although it is an anisotropic chain-silicate. The only visible indication of the anisotropy of diopside is the local presence of indentation at the pristine-retrogressed limit, due to limited fluid infiltration along cleavage surfaces.

6.3. Reliability of the conclusions

The above conclusions are based on a detailed study of structures surrounding a single uranothorianite grain. The representativity of the studied zone can then be legitimately questioned. Many features observed around this particular grain are visible in the whole thin section, such as the radiating cracks, the presence of retrogressed zone along the diopside–uranothorianite interface, and the presence of a porous layer along the calcite–uranothorianite. Those features are also present in all studied samples of the same rock. Observations at the nano-scale by coupling FIB/TEM analyses, like the presence of a wide amorphous zone along the calcite–uranothorianite boundary, or the presence of chains of ThO$_2$ crystals, which are time-consuming, cannot easily be multiplied all around a thin section, but are regular in shape and size, and are in agreement with damage model. Therefore we are quite confident that these are general features in this sample. Moreover, similar observations have been reported in other studies (Seydoux-Guillaume et al., 2003, 2007; Nasdala et al., 2006; Seydoux-Guillaume, unpublished), suggesting that it is common in rocks containing radioactive minerals. Some observations are clearly accidental, and may not be representative, such as the presence of zirconolite grains in the fractures.

6.4. Reliability of the model

In this study the SRIM/TRIM model provided several important constraints. This software has the advantage of being the most

sophisticated program available for non-specialist; on the other hand it has some limitations; for example it considers all materials as isotropic, and neglects the effect of crystalline structures. However, the fact that the size of damaged area in diopside is constant whatever its orientation provides an *a posteriori* justification of this assumption. Diopside is a chain-based, highly anisotropic structure, and if radiation damage is sensitive to crystal anisotropy, it should be visible in this mineral.

7. Conclusions

Radiohalos are complex structures, which deserve detailed study. Since radiation damage has a visible effect at the thin section scale, but also affects the structure of crystals at the atomic scale, studies must be conducted with a variety of techniques, including FIB/TEM for the nano-scale. Radiohalos are unique sources of information for understanding the behavior of minerals submitted to irradiation damages, even for non-radioactive minerals. This approach allows to study the effects of long-term irradiation and is thus very complementary to other methods that involve doping experiments with short-lived isotopes, which are far more expensive.

In the present study we have demonstrated the high resistance of uranothorianite to self-irradiation damage, in agreement with previous results (Evron et al., 1994), and, by contrast, the high sensitivity of diopside to radiation damage from neighbouring uranothorianite. TRIM/SRIM simulations have been shown to be able to correctly simulate radiation damage, even in complex minerals such as diopside.

Finally, we would like to emphasize that radiohalos are actually a point of chemical and mechanical weakness in a rock and probably a starting point for alteration.

References

Balan, E., Allard, T., Fritsch, E., Sélo, M., Falguères, C., Chabaux, F., Pierret, M.P., Calas, G., 2005. Formation and evolution of lateritic profiles in the middle Amazon basin: insights from radiation-induced defects in kaolinite. Geochimica et Cosmochimica Acta 69, 2193–2204.

Begg, B., Hess, N.J., Weber, W.J., Conradson, S.D., Scheiger, M.J., Ewing, R.C., 2000. XAS and XRD study of annealed ^{238}Pu and ^{239}Pu substituted zircons (Zr$_{0.92}$Pu$_{0.08}$SiO$_4$). Journal of Nuclear Materials 278, 121–224.

Black, L.P., Fitzgerald, J.D., Harley, S.L., 1984. Pb isotopic composition, colour, and microstructure of monazites from a polymetamorphic rock in Antarctica. Contrib. Mineral. Petrol. 85, 141–148.

Boulvais, P., Fourcade, S., Gruau, G., Moine, B., Cuney, M., 1998. Persistence of premetamorphic C and O isotopic signatures in marbles subject to Pan-African granulite facies metamorphism and U–Th mineralization (Tranomaro, South East Madagascar). Chemical Geology 150, 247–262.

Boulvais, P., Fourcade, S., Moine, B., Gruau, G., Cuney, M., 2000. Rare-earth elements distribution in granulite-facies marbles: a witness of fluid–rock interaction. Lithos 53, 117–126.

Burakov, B.E., Hanchar, J.M., Garbusov, V.M., Zirlin, V.A., 2002. Synthesis and investigation of Pu doped single crystal zircon ZrPuSiO$_4$. Radiochimica acta 90, 95–97.

Crocombette, J.P., Ghaleb, D., 2001. Molecular dynamics modeling of irradiation damage in pure and uranium doped zircon. Journal of Nuclear Materials 295, 167–178.

Davis, D.W., Krogh, T.E., 2000. Preferential dissolution of ^{234}U and radiogenic Pb from α-recoil-damaged lattice sites in zircon: implications for thermal histories and Pb isotopic fractionation in the near surface environment. Chemical Geology 172, 41–58.

Evron, R., Kimmel, G., Eyal, Y., 1994. Thermal recovery of self-radiation damage in uraninite and thorianite. Journal of Nuclear Materials 217, 54–66.

Ewing, R.C., 1975. The crystal chemistry of complex niobium and tantalum oxides IV. The metamict state: discussion. American Mineralogist 60, 728–733.

Ewing, R.C., 1994. The metamict state: 1993—the centennial. Nuclear Instruments and Methods in Physics Research B91, 22–29.

Ewing, R.C., Wang, L.M., 2002. Phosphates as nuclear waste forms. In: Kohn, M.J., Rakovan, J., Hughes, J.M., Ribbe, P.H. (Eds.), Phosphates: Geochemical, Geobiological and Materials Importance. . Reviews in Mineralogy and Geochemistry, vol. 48. Mineralogical Society of America, pp. 673–699.

Ewing, R.C., Weber, W.J., Clinard Jr., F.W., 1995. Radiation effects in nuclear waste forms. Progress in Nuclear Energy 29, 63–127.

Ewing, R.C., Chakoumakos, B.C., Lumpkin, G.R., Murakami, T., Greegor, R.B., Lytle, F.W., 1988. Metamict minerals: natural analogues for radiation damage effects in ceramic nuclear waste forms. Nuclear Instruments and Methods in Physics Research B32, 487–497.

Ewing, R.C., Meldrum, A., Wang, L.M., Wang, S.X., 2000. Radiation-induced amorphi-satio. In: Redfern, S.A.T., Carpenter, M.A., Ribbe, P.H. (Eds.), Transformation Processes in Minerals. . Reviews in Mineralogy and Geochemistry, vol. 39. Mineralogical Society of America, pp. 319–361.

Ewing, R.C., Meldrum, A., Wang, L.M., Weber, W.J., Corrales, L.R., 2003. Radiation damage in zircon. In: Hanchar, J.M., Hoskin, P.W.O. (Eds.), Zircon. . Reviews in Mineralogy and Geochemistry, vol. 53. Mineralogical Society of America, pp. 387–425.

Farges, F., 1997. Coordination of $Ti4+$ in silicate glasses: A high-resolution XANES spectroscopic study at the Ti K edge. Am. Mineral. 82, 36–43.

Farges, F., Calas, G., 1991. Structural analysis of irradiation damage in zircon and thorite. An X-ray absorption spectroscopic study. American Mineralogist 76, 60–73.

Farges, F., Ewing, R.C., Brown, G.E., 1993. The structure of aperiodic, metamict (Ca,Th)ZrTi2O7 (zirconolite): an EXAFS study of the Zr, Th and U sites. Journal of Material Research 8, 1983–1995.

Farnan, I., Balan, E., Pickard, C.J., Mauri, F., 2003. The effect of radiation damage on local structure in the crystalline fraction of $ZrSiO_4$: investigating the Si-29 NMR response to pressure in zircon and reidite. American Mineralogist 88, 1663–1667.

Gentry, R.V., 1973. Radioactive halos. Annual review in Nuclear Science 23, 347–362.

Gentry, R.V., 1974. Radiohalos in a radiochronological and cosmological perspective. Science 184, 62–66.

Harfouche, M., Farges, F., Crocombette, J.-P., Flank, A.-M., 2005. XAFS and molecular dynamics study of the structural environment around actinides and network formers in natural minerals analogues of ceramics for nuclear waste storage. Physica Scripta T115, 928–930.

Hawthorne, F.C., Groat, L.A., Raudsepp, M., Ball, N.A., Kimata, M., Spike, F.D., Gaba, R., Halden, N.M., Lumpkin, G.R., Ewing, R.C., Greegor, R.B., Lytle, F.W., Ercit, T.S., Rossman, G.R., Wicks, F.J., Ramik, R.A., Sherriff, B.L., Fleet, M.E., McCammon, C., 1991. Alpha-decay damage in titanite. American Mineralogist 76, 370–396.

Headley, T.J., Ewing, R.C., Haaker, R.F., 1981. Amorphous structure of metamict minerals observed by TEM. Nature 293, 449–450.

Heisbourg, G., Hubert, S., Dacheux, N., Ritt, J., 2003. The kinetics of dissolution of $Th_{1-x}U_xO_2$ solid solutions in nitric media. Journal of Nuclear Materials 321, 141–151.

Heisbourg, G., Hubert, S., Dacheux, N., Purans, J., 2004. Kinetic and thermodynamic studies of the dissolution of thoria-urania solid solutions. Journal of Nuclear Materials 335, 5–13.

Janeczek, J., Eby, R.K., 1993. Annealing of radiation damage in allanite and gadolinite. Physics and Chemistry of Minerals 19, 343–356.

Janeczek, J., Ewing, R.C., Oversby, V.M., Werme, L.O., 1996. Uraninite and UO_2 in spent nuclear fuel: a comparison. Journal of Nuclear Materials 238, 121–130.

Joly, J., 1907. Pleochroic halos. Philosophical Magazine 13, 381–383.

Lumpkin, G.R., Chakoumakos, B.C., 1988. Chemistry and radiation effects of thorite-group minerals from the Harding pegmatite, Taos County, New Mexico. American Mineralogist 73, 1405–1419.

Lumpkin, G.R., Ewing, R.C., 1988. Alpha decay damage in minerals of the pyrochlore group. Physics and Chemistry of Minerals 16, 2–20.

Lumpkin, G.R., Chakoumakos, B.C., Ewing, R.C., 1986a. Mineralogy and radiation effects of microlite from the Harding Pegmatite, Taos County, New Mexico. American Mineralogist 71, 569–588.

Lumpkin, G.R., Ewing, R.C., Chakoumakos, B.C., Greegor, R.B., Lytle, F.W., Forltyn, E.M., Clinard Jr., F.W., Boatner, L.A., Abraham, M.M., 1986b. Alpha-recoil damage in zirconolite (CaZrTi2O7). Journal of Material Research 1, 564–576.

Lumpkin, G.R., Eby, R.K., Ewing, R.C., 1991. Alpha-recoil damage in titanite (CaTiSiO5): direct observation and annealing study using high resolution transmission electron microscopy. Journal of Material Research 6, 560–564.

Linberg, M.L., Ingram, B., 1964. Rare-earth silicatian apatite from the Adirondack Mountains, New-York. US Geological Survey Professional Paper 501-B, B64–B65.

Matzke, H.j., Turos, A., 1992. Ion implantation studies of UO_2 and UN. Journal of Nuclear Materials 188, 285–292.

Matzke, H.j., Wang, L.M., 1996. High-resolution transmission electron microscopy of ion irradiated uranium oxide. Journal of Nuclear Materials 231, 155–158.

Meldrum, A., Boatner, L.A., Weber, W.J., Ewing, R.C., 1998. Radiation damage in zircon and monazite. Geochimica et Cosmochimica Acta 62, 2509–2520.

Meldrum, A., Zinckle, S.J., Boatner, L.A., Ewing, R.C., 1999. Heavy-ion irradiation effects in the ABO4 orthosilicates: decomposition, amorphization, and recrystallization. Physical Review B59, 3981–3992.

Meunier, J.D., Sellier, E., Pagel, M., 1990. Radiation damage rims in quartz from uranium bearing sandstones. Journal of Sedimentary Petrology 60, 53–58.

Moine, B., Rakotondratsima, C., Cuney, M., 1985. Les pyroxénites à urano-thorianite du sud-est de Madagascar, conditions physico-chimiques de la métasomatose. Bulletin de Minéralogie 108, 325–340.

Moine, B., Ramambazafy, A., Rakotondrazafy, M., Ravololomiandrinarivo, B., Cuney, M., de Parseval, P., 1998. The role of fluorine-rich fluids in the formation of the thorianite and sapphire deposits of S.E. Madagascar. 8th Goldschmidt Conference. Mineralogical Magazine, vol. 62A, pp. 999–1000.

Mügge, O., 1907. Radioaktivität als Ursache der pleochroitischen Höfe. Zentralblatt Mineralogie Geologie 71, 529–532.

Murakami, T., Chakoumakos, B.C., Ewing, R.C., Lumpkin, G.R., Weber, W.J., 1991. Alpha-decay event damage in zircon. Am. Mineral. 76, 1510–1532.

Nasdala, L., Irmer, G., Wolf, D., 1995. The degree of metamictization in zircons a Raman spectroscopic study. European Journal of Mineralogy 7, 471–478.

Nasdala, L., Wenzel, M., Andrut, M., Wirth, R., Blaum, P., 2001. The nature of radiohaloes in biotite: experimental studies and modeling. American Mineralogist 86, 498–512.

Nasdala, L., Wildner, M., Wirth, R., Groshopf, N., Pal, D.C., Möller, A., 2006. Alpha particle haloes in chlorite and cordierite. Mineralogy and Petrology 86, 1–27.

Odom, A.L., Rink, W.L., 1989. Giant radiation-induced colored halos in quartz solution to a riddle. Science 246, 107–109.

Ouchani, S., Dran, J.C., Chaumont, J., 1997. Evidence of ionization annealing upon helium-ion irradiation of pre-damaged fluorapatite. Nuclear Instruments and Methods. Physical Research, vol. B132, pp. 447–451.

Overwijk, M.H.F., van den Heuvel, F.C., Bulle-Lieuwma, C.W.T., 1993. Novel scheme for the preparation of transmission electron microscopy specimens with a focused ion beam. Journal of Vacuum Science and Technology 11, 202.

Owen, M.R., 1988. Radiation damage halos in quartz. Geology 16, 529–532.

Paquette, J.L., Nédélec, A., Moine, B., Rakotondrazafy, M., 1994. U–Pb, single zircon evaporation and Sm–Nd isotopic study of a granulite domain in SE Madagascar. Journal of Geology 102, 523–538.

Rakotondratsima, C., 1983. Les pyroxénites à Uranothorianite du Sud-Est de Mada-gascar: étude pétrographique, minéralogique et géochimique. Thesis, Claude Bernard University-Lyon, 226 pp.

Rakotondrazafy, M., 1995. La hibonite (CaAl12O19) du Sud-Est de Madagascar. Caractères et modalités de formation dans les skarns à thorianite du faciès granulite (Unpublished). Thesis, Antananarivo University, Madagascar.

Rakotondrazafy, M., Moine, B., Cuney, M., 1996. Mode of formation of hibonite (CaAl12O19) within the U–Th skarns from the granulites of S–E Madagascar. Contribution to Mineralogy and Petrology 123, 190–201.

Ramambazafy, A., 1998. Granites et fluides en relation avec les skarns à thorianite dans les granulites du S.E. de Madagascar. Thesis, Paul Sabatier Toulouse III University, 302 pp.

Ramambazafy, A., Moine, B., Rakotondrazafy, M., Cuney, M., 1998. Signification des fluides carbonaques dans les granulites et les skarns du Sud-Est de Madagascar. Compte Rendu de l'académie des Sciences 327, 743–748.

Roberts, S., McCaffrey, J., Giannuzzi, L., Stevie, F., Zaluzec, N., 2001. Advanced techniques in TEM specimen preparation. In: Xiao-Feng, Zhang., Ze, Zhang (Eds.), Progress in transmission electron microscopy, vol. 1. Springer Series in Surface Sciences, 38, pp. 336–342.

Romer, R., 2003. Alpha-recoil in U–Pb geochronology: effective sample size matters. Contribution to Mineralogy and Petrology 145, 481–491.

Seydoux-Guillaume, A.M., Paquette, J.L., Wiedenbeck, M., Montel, J.M., Heinrich, W., 2002. Experimental resetting of the U–Th–Pb systems in monazite. Chemical Geology 191, 165–181.

Seydoux-Guillaume, A.M., Goncalves, P., Wirth, R., Deutsch, A., 2003. TEM study of polyphasic and discordant monazites: site specific specimen preparation using the Focused Ion Beam technique. Geology 31, 973–976.

Seydoux-Guillaume, A.M., Wirth, R., Deutsch, A., Schärer, U., 2004. Microstructure of 24 – 1928 Ma concordant monazites: implications for geochronology and nuclear waste deposits. Geochimica et Cosmochimica Acta 68, 2517–2527.

Seydoux-Guillaume, A.M., Wirth, R., Ingrin, J., 2007. Contrasting response of $ThSiO_4$ and monazite to natural irradiation. European Journal of Mineralogy 19, 7–14.

Trachenko, K.O., 2004. Understanding resistance to amorphization by radiation damage. Journal of Physics: Condensed Matter 16, 1491–1515.

Trachenko, K.O., Dove, M.T., Salje, E.K.H., 2001. Atomistics modeling of radiation dammage in zircon. Journal of Physics: Condensed Matter 13, 947–952.

Vance, E.R., Metson, J.B., 1985. Radiation damage in natural titanites. Physics and Chemistry of Minerals 12, 255–260.

Wang, L.M., Ewing, R.C., 1992. Ion beam induced amorphization of complex ceramic materials — minerals. Materials Research Society Bulletin 13, 38–44.

Weber, W.J., Ewing, R.C., Catlow, C.R.A., Diaz de la Rubia, T., Hobbs, L.W., Kinishita, C., Matzke, H.J., Motta, A.T., Nastasi, M., Salje, E.H.K., Vance, E.R., Zinkle, S.J., 1998. Radiation effects in crystalline ceramics for the immobilization of high-level nuclear waste and plutonium. Journal of Material Research 13, 1434–1484.

Weber, W.J., Ewing, R.C., Wang, L.M., 1994. The radiation-induced crystalline-to-amorphous transition in zircon. Journal of Materials Research 9, 688–698.

Wirth, R., 2004. Focused Ion Beam (FIB): a novel technology for advanced application of micro- and nanoanalysis in geosciences and applied mineralogy. European Journal of Mineralogy 16, 863–876.

Young, R.J., 1997. Application of the focused ion beam in materials characterization and failure analysis. Microstructural Science 25, 491–496.

Zhang, M., Salje, E.K.H., 2001. Infrared spectroscopic analysis of zircon: radiation damage and the metamict state. Journal of Physics: Condensed Matter 13, 3057–3071.

Zhang, M., Salje, E.K.H., Bismayer, U., Groat, L.A., Malcherek, T., 2002. Metamictization and recrystallization of titanite: an infrared spectroscopic study. American Mineralogist 87, 882–890.

Ziegler, J.F., 2006. SRIM: the stopping and range of ions in matter. Instruction Manual.